*J. Fluid Mech.* (1999), *vol.* 383, *pp.* 29–54. Printed in the United Kingdom



# Displacement of a two-dimensional immiscible droplet adhering to a wall in shear and pressure-driven flows

By ANTHONY D. SCHLEIZER AND ROGER T. BONNECAZE

Department of Chemical Engineering, The University of Texas at Austin, Austin, TX 78712, USA

(Received 24 June 1997 and in revised form 3 September 1998)

The dynamic behaviour and stability of a two-dimensional immiscible droplet subject to shear or pressure-driven flow between parallel plates is studied under conditions of negligible inertial and gravitational forces. The droplet is attached to the lower plate and forms two contact lines that are either fixed or mobile. The boundary-integral method is used to numerically determine the flow along and dynamics of the free surface. For surfactant-free interfaces with fixed contact lines, the deformation of the interface is determined for a range of capillary numbers, droplet to displacing fluid viscosity ratios, droplet sizes and flow type. It is shown that as the capillary number or viscosity ratio or size of the droplet increases, the deformation of the interface increases and above critical values of the capillary number no steady shape exists. For small droplets, and at low capillary numbers, shear and pressure-driven flows are shown to yield similar steady droplet shapes. The effect of surfactants is studied assuming a fixed amount of surfactant that is subject to convective–diffusive transport along the interface and no transport to or from the bulk fluids. Increasing the surface Péclet number, the ratio of convective to diffusive transport, leads to an accumulation of surfactant at the downstream end of the droplet and creates Marangoni stresses that immobilize the interface and reduce deformation. The no-slip boundary condition is then relaxed and an integral form of the Navier-slip model is used to examine the effects of allowing the droplet to slip along the solid surface in a pressure-driven flow. For contact angles less than or equal to 90°, a stable droplet spreads along the wall until a steady shape is reached, when the droplet translates across the wall at a constant velocity. The critical capillary number is larger for these droplets compared to those with pinned contact lines. For contact angles greater than 90°, the wetted area between a stable droplet and the wall decreases until a steady shape is reached. The critical capillary number for these droplets is less than that for pinned droplets. Above the critical capillary number the droplet completely detaches for a contact angle of 120°, or part of it is pinched off leaving behind a smaller attached droplet for contact angles less than or equal to 90°.

## 1. Introduction

The displacement of immiscible fluids is important in sub-surface processes such as enhanced oil recovery or the transport of non-aqueous phase liquids in the soil via water or surfactant flooding. The overall efficiency of these processes depends upon the ability to effectively transport fluids through the network of pores and

throats that make up the medium. In these processes there are several possible fluid–fluid displacement scenarios. Previous work on immiscible displacement in capillary tubes has focused on the displacement of a fluid meniscus (e.g. Cox 1986), the displacement of a freely suspended fluid droplet (e.g. Tsai & Miksis 1994; Manga 1996), the displacement of a suspension of fluid droplets (Zhou & Pozrikidis 1991), and the displacement of a freely suspended fluid droplet in the presence of surfactants (Borhan & Mao 1992).

Borhan & Mao (1992) comprehensively studied the deformation of axisymmetric droplets in straight capillaries and the effect of surfactants on the process at low Reynolds number using the boundary-integral method for a range of droplet sizes, droplet to fluid viscosity ratios $\lambda$, capillary numbers $Ca$ (a ratio of viscous to surface forces), surface Péclet numbers $Pe$ (a ratio of convection to diffusion of surfactant along the interface), and values of $\beta$ (a dimensionless quantity which is a measure of the sensitivity of the interfacial tension to variations in concentration of surfactant). Borhan & Mao found that the deformation of the droplet increases as $Ca$ or $\lambda$ increases. They also found that in the presence of surfactants the shape of the droplet is relatively insensitive to $Pe$. For $Pe$ in the range of 0.01 to 100, the maximum difference in the deformation of the interface, which they define as the arclength of the interface when the droplet has reached a steady shape normalized by its initial value, is approximately 5%. As a result of the insensitivity of the interface shape to $Pe$, variations in $\beta$ simply modify the surface tension of the interface and the effective capillary number of the system. They also found that for large $Pe$, the drop shape becomes independent of the viscosity ratio. For the lower viscosity ratios, Marangoni stresses immobilize the surface of the droplet and the internal flow is eliminated, while for higher viscosity ratios the surface velocity and internal flow are already very small regardless of the effects of surfactants.

While there has been a significant amount of work focused on the pressure-driven flow of freely suspended droplets (see Borhan & Mao 1992 for a review), the deformation of attached droplets has, until recently, received less attention. Much of the research on attached droplets has focused on conditions where there is no external flow and gravitational forces are responsible for deformation of a droplet. In a series of experiments in which droplets were placed on an inclined plane, Furmidge (1962) determined the critical inclination angle for which a droplet would remain attached. Dussan V. & Chow (1983) and Dussan V. (1985) developed a theoretical analysis of the problem for slender droplets and showed that the yield condition experimentally determined by Furmidge is an exact relationship. Milinazzo & Shinbrot (1988) numerically determined the shape of a three-dimensional droplet on a vertical wall for a range of Bond numbers $Bo$, the ratio of gravitational to surface forces, using a variational formulation of the problem combined with an arclength continuation method. They were interested in determining whether the wetted area of the drop could remain constant as $Bo$ was increased. They found that beyond a critical $Bo$ the droplet penetrated the plane wall, and they suggested that at this point either the wetted area must change or the droplet must begin to move. Tuck & Schwartz (1991) assumed that the wetted area changes when a critical $Bo$ is exceeded, and they present results for thin drops that have de-wetted the solid surface.

Dussan V. (1987) considered the effects of external flow over attached droplets. She determined the yield conditions for a slender droplet attached to a solid surface in a weak shear flow using a lubrication approximation. The maximum capillary number for which a stationary drop could be maintained was determined and found to depend on the value of the contact angle hysteresis (the difference between the advancing

and receding contact angles) and the advancing contact angle. The critical capillary number was found to be independent of the droplet viscosity, which only affects the time scale of the deformation.

Li & Pozrikidis (1996) used the boundary-integral method to study shear flow over an attached three-dimensional droplet. Gravitational effects were considered negligible and the fixed contact line was chosen to have either a circular or elliptical shape; thus, the variation in the contact angle around the contact line was determined as part of the solution. Droplet profiles were determined by following the dynamic behaviour of the interface until a steady shape was reached. The effects of capillary number, droplet volume and the shape of the contact line were examined. They found that larger droplets and elliptical contact lines resulted in lower critical capillary numbers for continuous deformation of the droplet. They also showed that attached droplets deform more than freely suspended droplets in an infinite shear flow, indicating that the presence of the wall promotes deformation.

Feng & Basaran (1994) studied the problem of shear flow over a two-dimensional bubble with contact lines pinned to a deep slot. The finite element method was combined with an iterative method to solve for the velocity field and the shape of the free surface. For a range of $Ca$ and Reynolds numbers $Re = \rho UL/\mu$ (a ratio of inertial to viscous forces), they found that the flow behind the droplet separates and the length of the eddy increases as $Re$ increases. The structure of the flow field was shown to depend only the Weber number $We = Re\,Ca$ (a ratio of inertial to surface forces). Their simulations were restricted to low $Ca$ and a yield condition based on $Ca$ was never determined. The inertial stresses, which scale as $We$, or the viscous stresses, which scale as $Ca$, can overcome the interfacial forces and dislodge a drop.

Recently, Dimitrakopoulos & Higdon (1997) determined the yield conditions for a two-dimensional droplet adhering to a plane solid surface in a shear flow and assuming contact angle hysteresis. The boundary-integral method was used to solve for the fluid flow and a modified Newton's method was used to determine the shape of the free surface. A wide range of $Ca$, $Bo$, viscosity ratios, and advancing and receding contact angle values were examined. Unlike the previous work for shear flow over attached droplets, the effects of gravity were examined and it was shown that as gravitational forces increase, the critical $Ca$ for continuous deformation of the droplet decreases. They also found that the behaviour of viscous and inviscid droplets is qualitatively different. Increasing the advancing contact angle for viscous drops leads to an increase in the critical capillary number, while for inviscid drops it leads to a decrease in the critical capillary number. They also demonstrated that the range of validity of the lubrication equations that are often used to solve problems for thin drops is quite small.

In this paper the dynamic behaviour and stability of a two-dimensional liquid drop between parallel plates in a shear or pressure-driven flow in the absence of inertial and gravitational forces is studied. Unlike previous work on attached droplets, the no-slip boundary condition at the contact lines is relaxed to examine the effect of allowing the droplet to slip. The effects of surfactants on the dynamics and stability of a droplet with fixed contact lines are also examined.

The outline for the paper is as follows. In § 2 the boundary-integral formulation for this problem is developed and the boundary conditions and details of the numerical scheme are presented. In § 3 results are presented for the deformation and stability of a droplet where the no-slip boundary condition is enforced and the contact lines remain pinned to their initial positions. For these simulations the contact angle is determined as part of the solution procedure. The effects of capillary number, viscosity

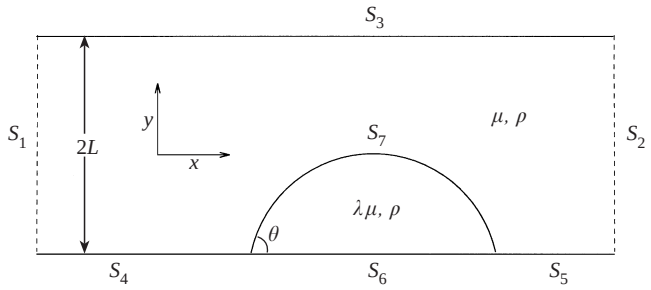


FIGURE 1. Schematic of an attached droplet between two flat plates. The fluid between the plates is subject to a shear flow by translating the upper plate $S_3$ or a pressure-driven flow by specifying a parabolic velocity profile and at the inlet and outlet, $S_1$ and $S_2$, respectively.

ratio, droplet size and flow regime on deformation and stability of the droplet are examined. For small droplets and at low capillary numbers shear- and pressure-driven flows are shown to yield similar steady droplet shapes. If surfactants are present, it is shown that as the surface Péclet number increases the deformation of the droplet decreases due to Marangoni stresses caused by a non-uniform surfactant distribution along the interface. In § 4 the effect of relaxing the no-slip condition on the contact lines is examined. While there have been a number of studies on spreading droplets with moving contact lines (e.g. Hocking & Rivers 1982; Haley & Miksis 1991), the previous studies on deformation of attached droplets in shear flows have only considered pinned contact lines. The slip model used is an integral form of the Navier-slip model. Since the droplet is allowed to slip, the contact angle at the contact line is specified. The steady and unsteady droplet shapes are found to be considerably different than those for which the contact lines are pinned. Specifically, the wetted area between the droplet and wall is shown to increase or decrease depending on the values of capillary number and the contact angle. In § 5 a summary of the results and suggestions for future directions for work on the displacement of attached droplets is presented.

## 2. Mathematical formulation and numerical method

### 2.1. *Mathematical formulation*

Consider the steady displacement of a two-dimensional droplet with area $A$ between two flat plates which are located at $y = \pm L$ (figure 1). The droplet is attached to the lower plate and forms two contact lines at $x_1$ and $x_2$. The contact angle $\theta$ is measured through the droplet. The droplet is subjected to a shear- or pressure-driven flow by moving the upper plate with a prescribed velocity or imposing a macroscopic pressure gradient. Both the displacing fluid and the droplet are incompressible and Newtonian and have viscosities $\mu$ and $\lambda\mu$, respectively, and densities $\rho$. In what follows all lengths are made dimensionless by the half-width of the channel $L$, velocities by $U = Eh$, where $E$ is the shear rate at the wall and $h$ is the initial height of the droplet, and pressures and stresses by $\mu U/L$.

In the absence of inertial forces, the fluid flow is governed by Stokes equations, which in dimensionless form are given by

$$\nabla \cdot \boldsymbol{T} = 0 \quad \text{and} \quad \nabla \cdot \boldsymbol{u} = 0, \tag{2.1}$$

where the stress tensor $\boldsymbol{T} = -p\boldsymbol{I} + (\nabla \boldsymbol{u} + \nabla \boldsymbol{u}^T)$, $p$ is the pressure, $\boldsymbol{u}$ is the velocity and

$\boldsymbol{I}$ is the idem tensor. The equations for Stokes flow have an integral representation which is convenient for solving free-surface problems and is used to model the problem at hand. The integral representation of Stokes equation relates the velocity at a destination point $\boldsymbol{x}$ to the force densities and velocities at source points $\boldsymbol{y}$ and is given by

$$\frac{1}{4\pi}\int_{\partial\Omega}[\boldsymbol{J}(\boldsymbol{x},\boldsymbol{y})\cdot\boldsymbol{f}(\boldsymbol{y})-\boldsymbol{u}(\boldsymbol{y})\cdot\boldsymbol{K}(\boldsymbol{x},\boldsymbol{y})\cdot\boldsymbol{n}(\boldsymbol{y})]\ \mathrm{d}S(\boldsymbol{y})=\begin{cases}\boldsymbol{u}(\boldsymbol{x}), & \boldsymbol{x}\in\Omega,\\ \frac{1}{2}\boldsymbol{u}(\boldsymbol{x}), & \boldsymbol{x}\in\partial\Omega,\\ 0, & \boldsymbol{x}\notin\Omega,\end{cases}\tag{2.2}$$

where $\partial\Omega$ is the boundary of the domain of interest, $\Omega$ is the interior of the domain, $\boldsymbol{n}$ is the outwardly directed unit normal, and $\boldsymbol{f}=\boldsymbol{n}\cdot\boldsymbol{T}$ is the force density. A detailed derivation of this equation is given, for example, by Pozrikidis (1992). The free–space Green's functions or kernels for Stokes flow, $\boldsymbol{J}$ and $\boldsymbol{K}$, map the force and velocity at $\boldsymbol{y}$ to the velocity at $\boldsymbol{x}$ and represent the solution to a point-force singlet and doublet (e.g. Tanzosh, Manga & Stone 1992). For a two-dimensional unbounded domain, they are given by

$$\boldsymbol{J}=\boldsymbol{I}\ln r-\frac{\boldsymbol{rr}}{r^2}\quad\text{and}\quad\boldsymbol{K}=4\frac{\boldsymbol{rrr}}{r^4},\tag{2.3}$$

where $\boldsymbol{r}=\boldsymbol{x}-\boldsymbol{y}$ and $r=|\,\boldsymbol{r}\,|$.

To obtain an expression for velocities and forces in the domain, the integral representation for Stokes flow is first written for points both inside and outside the droplet, that is,

$$\frac{1}{4\pi}\int_{\partial\Omega}[\boldsymbol{J}(\boldsymbol{x},\boldsymbol{y})\cdot\boldsymbol{f}(\boldsymbol{y})-\boldsymbol{u}(\boldsymbol{y})\cdot\boldsymbol{K}(\boldsymbol{x},\boldsymbol{y})\cdot\boldsymbol{n}(\boldsymbol{y})]\ \mathrm{d}S(\boldsymbol{y})=\begin{cases}\boldsymbol{u}(\boldsymbol{x}), & \boldsymbol{x}\in\Omega_t,\\ \frac{1}{2}\boldsymbol{u}(\boldsymbol{x}), & \boldsymbol{x}\in\partial\Omega_t,\\ 0, & \boldsymbol{x}\notin\Omega_t,\end{cases}\tag{2.4}$$

$$\frac{1}{4\pi}\int_{\partial\Omega}[\boldsymbol{J}(\boldsymbol{x},\boldsymbol{y})\cdot\boldsymbol{f}(\boldsymbol{y})-\lambda\boldsymbol{u}(\boldsymbol{y})\cdot\boldsymbol{K}(\boldsymbol{x},\boldsymbol{y})\cdot\boldsymbol{n}(\boldsymbol{y})]\ \mathrm{d}S(\boldsymbol{y})=\begin{cases}\lambda\boldsymbol{u}(\boldsymbol{x}), & \boldsymbol{x}\in\Omega_d,\\ \frac{1}{2}\lambda\boldsymbol{u}(\boldsymbol{x}), & \boldsymbol{x}\in\partial\Omega_d,\\ 0, & \boldsymbol{x}\notin\Omega_d.\end{cases}\tag{2.5}$$

Here, $\Omega_t$ is the domain bounded by the tube walls and the inlet and outlet planes except for the domain of the droplet, $\Omega_d$. These equations are summed to yield an integral formulation which is valid over the entire domain. Along the boundary, the velocity is given by

$$\begin{aligned}\mathscr{C}\boldsymbol{u}=\frac{1}{4\pi}\int_{\partial\Omega}(\boldsymbol{J}\cdot\boldsymbol{f}-\boldsymbol{u}\cdot\boldsymbol{K}\cdot\boldsymbol{n})\ \mathrm{d}S+\frac{1}{4\pi}\int_{S_6}(\boldsymbol{J}\cdot\boldsymbol{f}-\lambda\boldsymbol{u}\cdot\boldsymbol{K}\cdot\boldsymbol{n})\ \mathrm{d}S\\ -\frac{1}{4\pi}\int_{S_7}(\boldsymbol{J}\cdot\Delta\boldsymbol{f}+(1-\lambda)\boldsymbol{u}\cdot\boldsymbol{K}\cdot\boldsymbol{n})\ \mathrm{d}S,\end{aligned}\tag{2.6}$$

where here $\partial\Omega$ includes surfaces $S_1$–$S_5$ in figure 1 and

$$\mathscr{C}=\begin{cases}\frac{1}{2} & \text{for}\quad\boldsymbol{x}\in\partial\Omega,\\ \frac{1}{2}(\lambda+1) & \text{for}\quad\boldsymbol{x}\in S_7,\\ \frac{1}{2}\lambda & \text{for}\quad\boldsymbol{x}\in S_6.\end{cases}$$

The jump in force density across the interface, $\Delta \boldsymbol{f}$, is due to the curvature and variation in surface tension along the interface and is given by

$$\Delta \boldsymbol{f} = \frac{1}{Ca_c}[\nabla_s \gamma - \gamma \boldsymbol{n} \nabla_s \cdot \boldsymbol{n}]. \tag{2.7}$$

Here $\nabla_s = (\boldsymbol{I} - \boldsymbol{nn}) \cdot \nabla$ is the surface gradient operator, $\nabla_s \cdot \boldsymbol{n}$ is the curvature, the capillary number $Ca_c = \mu U/\gamma_c$ is a ratio of viscous to surface forces with $\gamma_c$ being the surface tension of the clean, surfactant-free interface. In the presence of surfactants, the surface tension can vary along the interface due to a non-uniform distribution of surfactant, i.e. $\gamma = \gamma(\Gamma)$, where $\Gamma$ is the dimensionless concentration of surfactant on the interface. Note that $\gamma$ has been non-dimensionalized by $\gamma_c$, and $\Gamma$ has been non-dimensionalized by $\Gamma_0$, the initial uniform concentration of surfactant. The equation for the jump in force density across the interface can now be written as

$$\Delta \boldsymbol{f} = \frac{1}{Ca_c}\left[\left(\frac{\mathrm{d}\gamma}{\mathrm{d}\Gamma}\right)\nabla_s \Gamma - \gamma \boldsymbol{n} \nabla_s \cdot \boldsymbol{n}\right]. \tag{2.8}$$

An equation of state relating $\gamma$ and $\Gamma$ must be specified. Here the simulations are restricted to situations where the surfactant is present in dilute concentrations and a linear relationship between the concentration of surfactant and surface tension exists: $\gamma = 1 - \beta\Gamma$. The parameter $\beta$ is a measure of the sensitivity of the surface tension to concentration of surfactant and is given by $\beta = \Gamma_0 RT/\gamma_c$ (e.g. Borhan & Mao 1992), where $R$ is the gas constant and $T$ is the absolute temperature. Substituting this expression for $\gamma$, the following equation for the jump in force density across the interface is obtained:

$$\Delta \boldsymbol{f} = \frac{1}{Ca(1-\beta)}[-\beta \nabla_s \Gamma - (1 - \beta\Gamma)\boldsymbol{n} \nabla_s \cdot \boldsymbol{n}]. \tag{2.9}$$

The new capillary number, $Ca = \mu U/\gamma_c(1-\beta)$, is based on the equilibrium value of the surface tension for an interface with a uniform distribution of surfactant. A convection–diffusion equation for surfactant transport along the interface is used to determine the distribution of surfactant along the interface assuming no transport of surfactant to or from the ambient fluid, and is given by (Stone 1990)

$$\frac{\partial \Gamma}{\partial t} + \nabla_s \cdot \left(\boldsymbol{u}_s \Gamma - \frac{1}{Pe}\nabla_s \Gamma\right) + \Gamma(\nabla_s \cdot \boldsymbol{n})(\boldsymbol{u} \cdot \boldsymbol{n}) = 0, \tag{2.10}$$

where $\boldsymbol{u}_s = (\boldsymbol{I} - \boldsymbol{nn}) \cdot \boldsymbol{u}$ is the surface velocity. The surface Péclet number $Pe = UL/D_S$ is the ratio of convection to diffusion of surfactant along the interface, where $D_S$ is the surface diffusivity. The first three terms of this equation are the standard accumulation, convection and diffusion terms for the transport of a scalar quantity. The last term is a source-like contribution due to the deformation of the interface. Along the interface there is no-flux of surfactant at the contact lines and the total amount of surfactant on the interface remains constant. The first boundary condition assumes that no surfactant is deposited along or adsorbed from the solid surface. The second condition is due to the two no-flux conditions at the contact lines and because the surfactant is assumed to be insoluble.

The surface of the drop evolves according to the kinematic condition

$$\frac{\mathrm{d}\boldsymbol{x}_s}{\mathrm{d}t} = \boldsymbol{u}(\boldsymbol{x}_s), \tag{2.11}$$

where $\boldsymbol{x}_s$ represents points along the interface.

There is no flow through the top and bottom plates, and so $\boldsymbol{u} \cdot \boldsymbol{n} = 0$. The no-slip boundary condition is imposed along the top plate, and so $\boldsymbol{u} \cdot \boldsymbol{t} = 0$ for pressure-driven flow or $\boldsymbol{u} \cdot \boldsymbol{t} = 2$ for shear flow, where $\boldsymbol{t}$ is the unit tangent along the wall. The tangential velocity on the bottom plate also vanishes, except perhaps at the contact lines.

At the inlet and outlet a constant average velocity between the plates is enforced and it is assumed that all disturbances due to the presence of the droplet have decayed, so that

$$\frac{1}{2}\int_{-1}^{1} u_x(y)\,\mathrm{d}y = G \quad \text{and} \quad u_y = 0, \tag{2.12}$$

where the $u_x$ and $u_y$ are the $x$ and $y$ components of the velocity, respectively. For shear flow $G = 1/h$ and $u_x(y) = (1/h)(1 + y)$, and for pressure-driven flow $G = 2/3h$ and $u_x(y) = (1/h)(1 - y^2)$.

At the contact line either the no-slip boundary condition is enforced and the contact angle is allowed to vary, or the contact angle is fixed and the contact-line velocity based on a slip law is determined. There are several approaches to account for slip along the solid surface, but the usual approach is to specify a slip model which relates the velocity of the fluid along the solid surface to other dependent variables in the problem. The most commonly used model is the Navier-slip model in which the velocity of the fluid everywhere along the wall or in a small region near the contact line is assumed to be proportional to the shear stress at the wall,

$$u = k\frac{\partial u}{\partial y}, \tag{2.13}$$

where $k$ is a slip coefficient. The Navier-slip condition has been used to model the spreading of droplets (e.g. Hocking 1982) and immiscible fluid displacement in straight capillaries (e.g. Cox 1986) for small capillary numbers using analytical methods. However, any numerical scheme which implements the Navier-slip model must have a very fine grid near the contact line to capture the effects of slip close to the wall. Navier-slip coefficients are typically considered to be in the range of $10^{-3}$ to $10^{-6}$, and it has been found that in order to obtain numerical convergence using a Navier-slip model, several elements, or collocation points, must be placed in a region of this size near the contact line (Lowndes 1980; Tilton 1988; Zhou & Sheng 1990).

It is not practical to use the Navier-slip model in conjunction with the boundary-integral method for two reasons. The singularities in the kernels make it computationally difficult to accurately determine the integrals with grid spacings less than about $10^{-2}$ along a free surface and $10^{-3}$ along a solid surface. This is because of the hardware limitation of the workstation used in this study which employs 16–digit double-precision variables. In addition, for the solution to be stable numerically, the time steps must be on the order of the capillary number times the length of the smallest element along the interface. Using a Navier-slip model with a slip coefficient of $10^{-3}$ would require a prohibitively large amount of computation time.

To circumvent these problems, an integral form of the Navier-slip model is used to determine the velocity of the contact lines. The velocity of the contact line is assumed to be proportional to the integral of the shear stress in a small region near the contact line. Specifically,

$$u_{cl} = \alpha F_{cl}, \tag{2.14}$$

where $F_{cl} = \int_{-\epsilon}^{\epsilon} \boldsymbol{f} \cdot \boldsymbol{t}\,\mathrm{d}l$, $\alpha$ is a slip coefficient and $\epsilon$ is a small number. With this

slip model, the numerical solution of the integral equations converges as long as the integral of the force in the region near the contact line remains constant as the grid is refined. This is true provided there is at least one element within the contact line region. As a result, this slip model allows for much larger grid spacings while still capturing the macroscopic behaviour of the system.

### 2.2. *Numerical method*

The numerical procedure relies on de-coupling the solution of the interfacial dynamics from the surfactant transport and can broken down into the following steps: discretization of the domain, approximation of the force density and velocity on the discretized domain, integration of the boundary integrals, solving for $\boldsymbol{u}$ and $\boldsymbol{f}$ along the boundary, updating the interface shape, and determining the surfactant distribution along the interface. This procedure is like that used by Borhan & Mao (1992), while the numerical details are based on the work of Muldowney (1989). Along the boundary of the domain, the unknown quantities are the radial force density and axial velocity on the inlet and outlet flow planes, the force densities on the upper and lower plates and the velocities along the interface of the droplet.

In the numerical scheme the inflow and outflow planes $S_1$ and $S_2$ are placed sufficiently far downstream from the droplet so that all disturbances due to the presence of the droplet have decayed. Typically, placing $S_1$ and $S_2$ at dimensionless distances of $-4$ and 4, respectively, were sufficient to satisfy this criterion. However, in instances where the interface was unstable the outlet flow plane was placed at a dimensionless distance of 6. Increasing the distances beyond these values had a negligible effect on the dynamic interface shapes. Each surface $S_1$–$S_7$, parameterized by a cubic spline, is discretized into a number of elements and the unknown force density and/or velocity on each element are approximated by a Lagrange polynomial. On the interface, uniformly sized elements are used. Elements on the wall are concentrated near the contact line. This requires fewer overall elements along the wall and affords increased numerical stability compared to a uniform distribution of elements.

Due to numerical limitations with collocating the interface, the smallest droplet that was studied had a height which was approximately 10% of the separation distance between the two plates. For droplets of this size, the effects of the upper plate are negligible and the flow closely resembles that of a semi–infinite shear flow over a droplet.

A variety of interpolating polynomials was examined on each of the surfaces. It was determined that piecewise quadratic elements along the inflow and outflow planes, piecewise linear elements along the walls and piecewise constant elements along the interface yield practically the same results as higher order elements but at a significantly lower computational cost and were therefore used for all of the simulations. The integrals in equation (2.6) are evaluated using an adaptive Simpson's rule scheme for the non-self-interactions between elements. Since the integrals in equation (2.6) contain integrable singularities, the self-interaction of an element is evaluated by subtracting out a small region near the singularity, performing the integral analytically in that region, and adding it to the numerically computed integral over the rest of the region. The numerical integrations for self-interactions are evaluated using a modified Gaussian quadrature in which the quadrature points are concentrated near $\boldsymbol{y} = \boldsymbol{x}$ (Muldowney 1989). Results indicated that 100 Gaussian quadrature points yielded sufficient accuracy for the integration of the singularities.

Discretizing the domain and integrating over each of the resulting elements leads to a dense matrix which is solved using LU-decomposition to determine the unknown

coefficients for the interpolating polynomials on each element. Once the unknowns are determined, the inlet and outlet pressures are adjusted so that the average velocity (equation (2.12)) is satisfied. The inlet and outlet pressures are adjusted such that $P_{out} = -P_{in}$ so that any numerical integration errors in the integration of the pressures over the inlet and outlet elements have the same value. With the velocities along the interface known, the locations of the spline points on the interface are updated using the kinematic condition. Once the new interface shape is known, a new distribution of surfactant is determined by integrating the surfactant convection–diffusion equation using a centrally-differenced Crank–Nicholson scheme. The droplet is considered to be at steady state when the change in arclength with respect to time is one-twentieth its maximum value and both contact line velocities are within 1% of their mean steady-state values. When the droplet reaches a steady shape the normal velocities on the interface are $O(10^{-3})$. Reducing the convergence criteria by an order of magnitude results in less than a 1% change in the arclength of the interface. The change in the drop volume and total amount of surfactant on the interface did not change significantly during the simulations, except near the critical capillary number. In these cases, the droplet shape and amount of surfactant were rescaled at each time step to ensure that the drop volume and the total amount of surfactant were conserved. If no steady state is reached the simulation is halted when the interface intersects the wall or pinch-off of the droplet occurs.

Simulations were performed to ensure that the numerical scheme converged under spatial and temporal resolution. If the time steps were less than or equal to the capillary number divided by twice the number of collocation points along the interface, $\Delta t \leqslant Ca/2N$, the simulations converged under temporal resolution. To converge under spatial resolution, there were several convergence criteria which had to be met. First, the elements near the contact line had to be concentrated near the contact line with the element closest to the contact line being at least as small as the contact line region $\epsilon$. The exact discretization scheme near the contact line as well as the discretization scheme outside a dimensionless distance of $\pm 0.5$ from the contact line had a negligible effect on the dynamics of the interface. The number of elements along the inlet and outlet planes did not affect the solution. Along the interface, if the elements were smaller than the slip coefficient, the solution was independent of the number of elements used and converged under spatial resolution.

The numerical procedure can be summarized as follows: 1. discretize the domain; 2. approximate $\boldsymbol{u}$ and $\boldsymbol{f}$ on the discretized domain using Lagrange polynomials as the basis functions; 3. integrate basis functions over each element; 4. solve for unknowns on each element; 5. adjust pressure to ensure a given flow rate in the channel and linearly re-scale $\boldsymbol{u}$ and $\boldsymbol{f}$; 6. update the droplet shape using the kinematic condition; 7. determine the new distribution of surfactant on the droplet; 8. continue from step 1 until the stopping criteria are met.

## 3. Fixed contact lines

The transient motion and deformation of the interface of a droplet attached to a solid surface depends on the parameters $Ca, \lambda, \beta, Pe$, the area of the droplet $A$ and the flow regime. The central objectives are to determine the magnitude of deformation for these parameters and the critical values above which no steady droplet shape is reached. Results are first presented for pressure-driven flows in which the no-slip boundary condition is strictly enforced and the contact lines remain pinned to their initial positions. The no-slip boundary condition is later relaxed for the contact lines

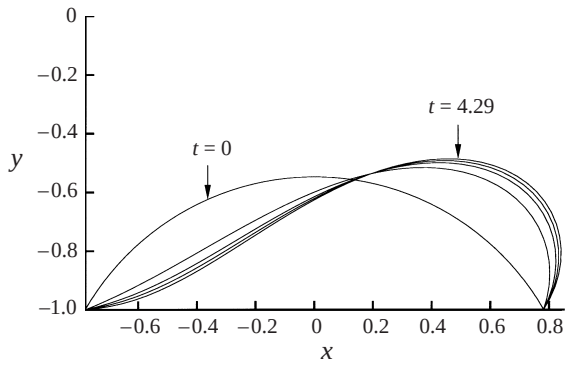


FIGURE 2. Evolution of the interface of an initially quiescent droplet in pressure-driven flow below its critical capillary number for times $t = 0$, 0.89, 1.77, 2.66 and 4.29 (steady state). Note the contact lines are pinned and that $Ca = 0.15$, $\theta = 60°$, $A = 0.5$, $\lambda = 1$.

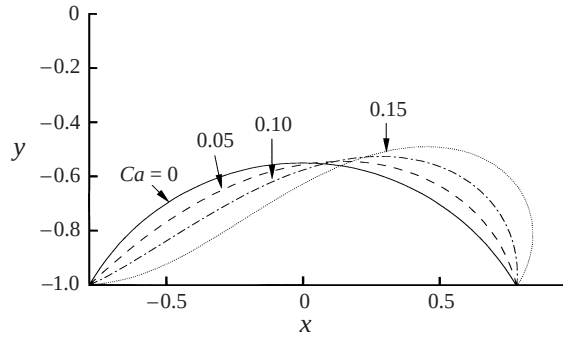


FIGURE 3. Steady-state interface of a droplet in pressure-driven flow for $Ca = 0.0$, 0.05, 0.10, 0.15. The contact lines are pinned and $\theta = 60°$, $A = 0.5$, $\lambda = 1$.

and the droplet is allowed to slip along the solid surface. For pinned droplets, no boundary condition on the contact angle is enforced at the contact lines. Enforcing the contact angle at the contact line does not significantly alter the overall droplet shape or the critical capillary number, and only affects the shape of the interface near the contact lines.

### 3.1. *Effect of Ca*

Figure 2 illustrates the time evolution of a droplet below its critical capillary number. In this particular simulation $Ca = 0.15$, the initial contact angle $\theta = 60°$, the viscosity ratio $\lambda = 1$ and the dimensionless droplet area $A = 0.5$. Initially, the droplet is a cylindrical cap, which upon application of the pressure gradient, deforms in the direction of the flow. In a dimensionless time of about $t = 4.29$ the droplet reaches a steady shape, when the viscous forces along the interface of the droplet due to the flow are balanced by surface forces. Note that the upstream contact angle decreases and the downstream contact angle increases due to the flow, which is generally true regardless of the initial contact angle. Figure 3 illustrates the steady-state shapes of droplets under the same conditions for capillary numbers ranging from $Ca = 0$ to 0.15. As the capillary number increases, the droplet deforms more due to the increase in viscous stresses along the interface. At a capillary number of 0.15 the droplet is close to being unstable as can be seen by the small upstream contact angle.

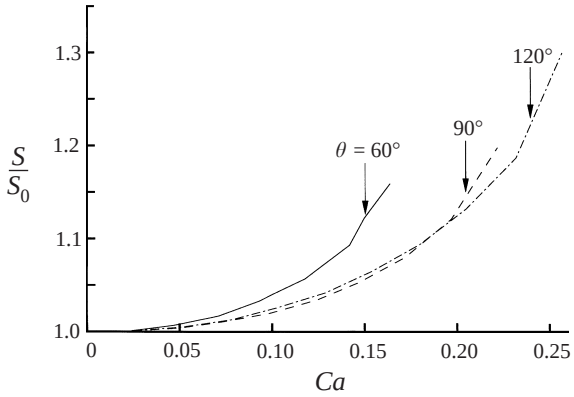


FIGURE 4. Ratio of the steady-state arclength of the interface to its initial value, $S/S_0$, or the deformation, versus capillary number $Ca$ for droplets with $\theta = 60°$, 90°, 120°, $A = 0.5$, $\lambda = 1$. The largest capillary number at the end of each curve corresponds to the critical capillary number above which no steady-state shape exists.

The results for low $Ca$ are qualitatively similar to those presented by Feng & Basaran (1994) and Li & Pozrikidis (1996) for droplets in shear flows. The droplets in figure 3 are sufficiently small that they experience essentially a shear flow and there is in fact quantitative agreement in the deformation and contact angles with those presented by Dimitrakopoulos & Higdon (1997). For example, for $Ca = 0.1$ in figure 3, the steady-state downstream or advancing contact angle is 90° and the upstream or receding contact angle is 29°. The capillary number computed by Dimitrakopoulos & Higdon (1997) for these contact angles in shear flow is also 0.1. (Note the capillary number defined by Dimitrakopoulos & Higdon (1997) must be multiplied by $h(\pi/A)^{1/2}$ to convert to the capillary number defined here.)

The deformation of a droplet over a range of $Ca$ is presented in figure 4 for contact angles of $\theta = 60°$, 90° and 120° with $\lambda = 1$ and $A = 0.5$. The deformation is defined as the steady-state arclength of the interfaces, $S$, divided by its initial value, $S_0$. The end of each curve corresponds to the critical capillary number beyond which no steady state exists. The critical capillary numbers in figure 4 range from approximately 0.16 to 0.26 and increase with increasing contact angle. Increasing the contact angle provides the upstream interface with a larger angle through which it can deform before penetrating the wall, which results in a higher critical capillary number. Above the critical capillary number the droplet continues to deform until the upstream portion of the interface near the contact line penetrates the capillary wall. This can be seen in figure 5 which illustrates the dynamic behaviour of droplets in pressure-driven flow above the critical capillary number for initial contact angles of $\theta = 60°$, 90° and 120°.

### 3.2. *Effect of droplet size*

Changing the droplet size is equivalent to changing the ratio of the initial height of the droplet to the distance between the plates. Figure 6 shows the dynamic behaviour and steady profiles for small ($A = 0.125$) and large ($A = 1$) droplets with $\theta = 60°$, $\lambda = 1$ and $Ca = 0.1$. Not surprisingly the larger droplet deforms more and takes longer to reach a steady shape. Figure 7 shows the effect of droplet size on deformation of a droplet under the same conditions. As the area of the droplet increases, the effect of the upper plate becomes increasingly more important because more fluid is pushed

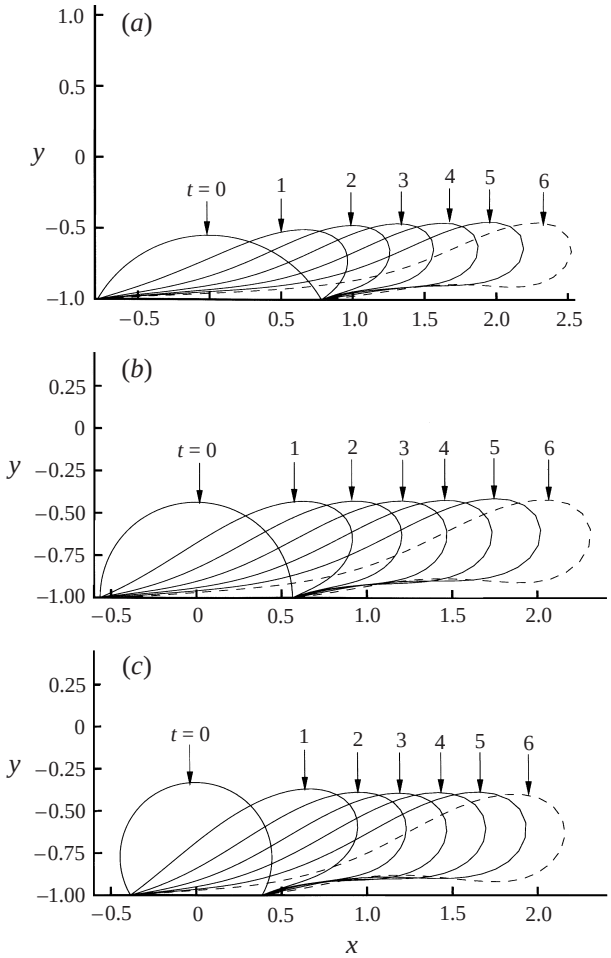


FIGURE 5. Evolution of the interfaces of an initially quiescent droplets in pressure-driven flow above their critical capillary numbers. The contact lines are pinned and $Ca = 0.4$, $A = 0.5$, $\lambda = 1$. (*a*) $\theta = 60^\circ$, (*b*) $\theta = 90^\circ$ and (*c*) $\theta = 120^\circ$, all at uniform time intervals from $t = 0$ to $t = 6.0$.

though an increasingly smaller gap, requiring a greater local pressure gradient and increasing deformation. Note that for $Ca = 0.1$, $\lambda = 1$ and $\theta = 60^\circ$ no steady shapes exist beyond a critical droplet area of $A = 1.5$.

### 3.3. *Effect of viscosity ratio*

Figures 8 and 9 illustrate the effect of viscosity ratio on the deformation of droplets with $\theta = 60^\circ$ and $A = 0.5$. In figure 8 the steady-state profiles of the droplet at $Ca = 0.1$ show that as the viscosity ratio between the droplet and displacing fluid increases, the deformation of the droplet increases. The droplet deforms due to pressure and shear stresses on its surface, and the latter increase for more viscous drops. Figure 9 illustrates the effect of viscosity ratio on the deformation of a medium sized droplet for a range of viscosity ratios. At a capillary number of 0.05 the deformation of the droplet increases from a value of $S/S_0 = 1.003$ at $\lambda = 0.125$ and does not increase significantly beyond a value of $S/S_0 = 1.013$ at $\lambda = 4$. However, at the larger capillary number of 0.1, the deformation increases from $S/S_0 = 1.013$ at $\lambda = 0.125$ and begins

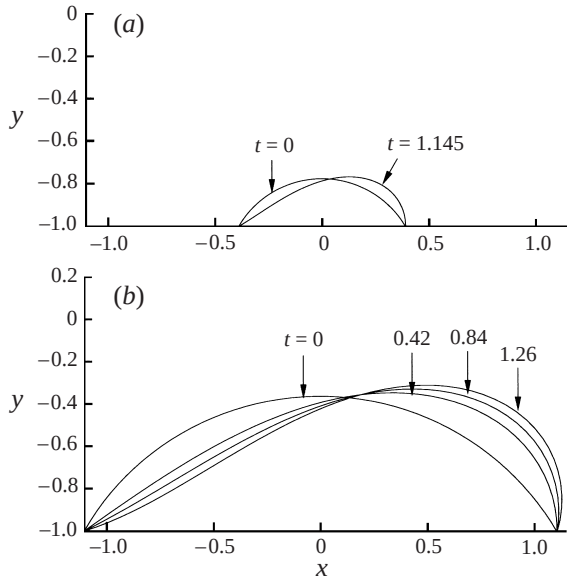


FIGURE 6. Evolution of the interfaces of small and large, initially quiescent droplets for $\theta = 60°$, $Ca = 0.1$, $\lambda = 1$. (*a*) $A = 0.125$ and $t = 0$ and 1.145; (*b*) $A = 1$ and at evenly spaced time intervals from $t = 0$ to 1.26. The longest times correspond to steady state.

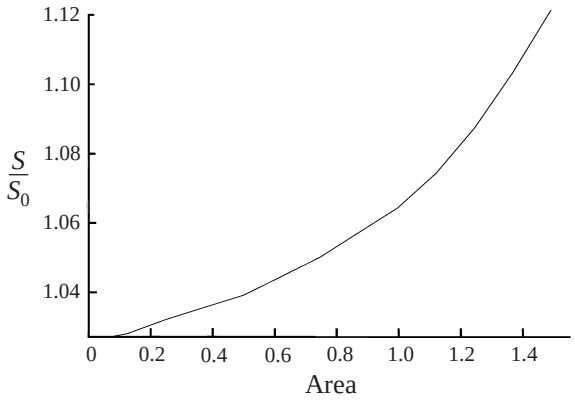


FIGURE 7. Steady-state deformation versus droplet size or area for $Ca = 0.1$, $\theta = 60°$ and $\lambda = 1$. Note that above $A = 1.5$, no steady droplet shape exists.

to plateau around a value of $S/S_0 = 1.073$ at $\lambda = 8$ but continues to increase slightly to $S/S_0 = 1.080$ at $\lambda = 20$. At low capillary numbers, the surface of the droplet is nearly immobilized by surface forces and the deformation is small regardless of the viscosity ratio. At higher capillary numbers, the surface velocity is larger and a larger viscosity ratio is required to immobilize the surface of the droplet.

Examination of table 1 shows that the critical capillary numbers for droplets in a pressure-driven flow with $\theta = 90°$ are 0.32, 0.22 and 0.17 for $\lambda = 0.125$, 1 and 8, respectively. This illustrates the general trend that increasing the viscosity ratio decreases the critical capillary number, which is again due to greater shear forces for more viscous drops. The results presented in table 1 are for an attached droplet in a

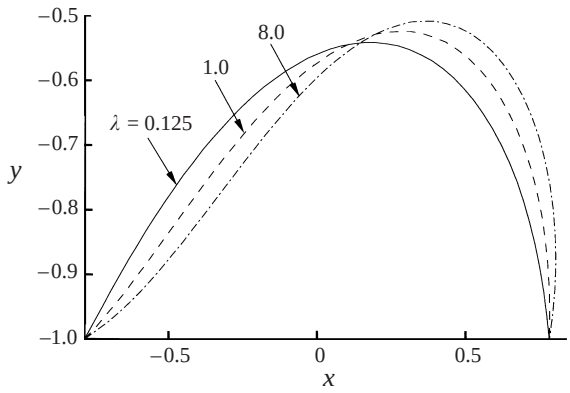


FIGURE 8. Effect of viscosity ratio on droplet deformation. Steady droplet shapes for $\lambda = 0.125$, 1.0, 8.0 and $Ca = 0.1$, $\theta = 60^\circ$, $A = 0.5$.

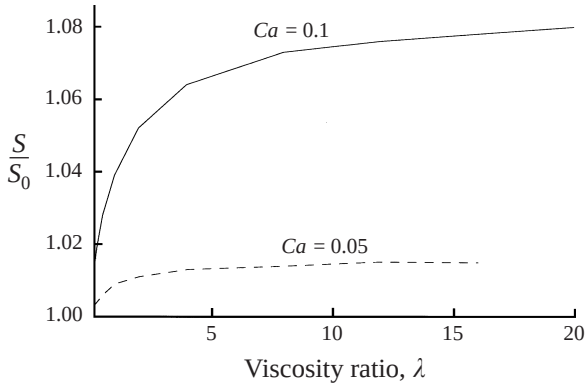


FIGURE 9. Effect of viscosity ratio on droplet deformation. Deformation versus viscosity ratio. $\theta = 60^\circ$, $A = 0.5$, $Ca = 0.05$, $Ca = 0.1$. The lowest value of the viscosity ratio $\lambda = 0.0625$.

| $Ca_{crit}$ | $\theta$ (deg.) | $\lambda$ | $A$ | $\beta$ | $Pe$ |
|---|---|---|---|---|---|
| 0.16 | 60 | 1.0 | 0.5 | 0 | X |
| 0.22 | 90 | 1.0 | 0.5 | 0 | X |
| 0.26 | 120 | 1.0 | 0.5 | 0 | X |
| 0.29 | 90 | 1.0 | 0.125 | 0 | X |
| 0.25 | 90 | 1.0 | 0.25 | 0 | X |
| 0.16 | 90 | 1.0 | 1.0 | 0 | X |
| 0.32 | 90 | 0.125 | 0.5 | 0 | X |
| 0.17 | 90 | 8.0 | 0.5 | 0 | X |
| 0.25 | 90 | 1.0 | 0.5 | 0.25 | 1.0 |
| 0.25 | 90 | 1.0 | 0.5 | 0.25 | 100.0 |
| 0.30 | 90 | 1.0 | 0.5 | 0.5 | 1.0 |
| 0.32 | 90 | 1.0 | 0.5 | 0.5 | 100.0 |

TABLE 1. Effect of contact angle $\theta$, viscosity ratio $\lambda$, droplet area $A$, surface Péclet number $Pe$ and $\beta$ on the critical capillary number $Ca_{crit}$ for pinned droplets in pressure-driven flow. When $\beta = 0$ there is no surfactant on the interface and the X denotes that $Pe$ is irrelevant.

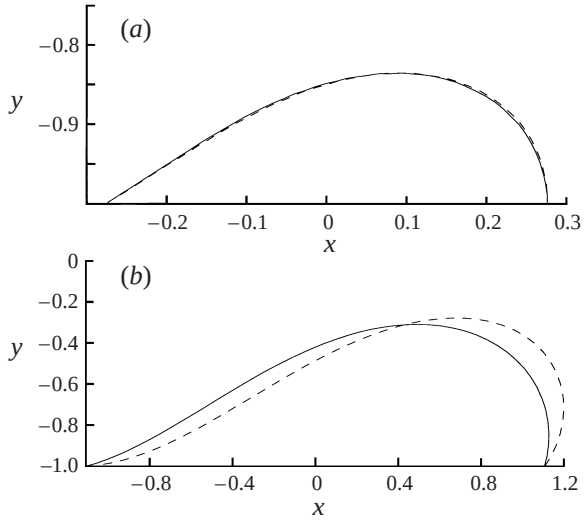


FIGURE 10. Effect of flow regime on droplet deformation. Steady droplet shapes of smaller and larger drops in shear (- - -) and pressure-driven (—) flow for $Ca = 0.1$, $\theta = 60^\circ$ and $\lambda = 1$. (*a*) Smaller drop, $A = 0.125$ and (*b*) larger drop $A = 1$.

pressure-driven flow. The critical capillary numbers for a droplet in a shear flow are approximately the same as those for a droplet in a pressure-driven flow.

### 3.4. *Effect of flow regime*

Figure 10 depicts the steady droplet profiles for two different–sized droplets in shear and pressure-driven flow with $Ca = 0.1$, $\theta = 60^\circ$ and $\lambda = 1$. When the droplets are small (figure 10*a*, $A = 0.125$), the shapes of the droplets for the two flow regimes are very similar because pressure-driven flow over a small droplet deviates little from a linear shear flow. The larger droplets (figure 10*b*, $A = 1$) both show a noticeable depression in the upstream portion of the interface. For the large droplet in the shear flow more fluid is pushed through a smaller gap which gives rise to a local pressure gradient and causes a deviation from the linear shear flow regime, thus creating the depression in the upstream portion of the interface. Figure 11 shows a comparison of the deformation of a medium sized droplet ($A = 0.5$) with $\lambda = 1$ for shear and pressure-driven flows. As the capillary number increases, the difference in the magnitude of the deformation increases.

### 3.5. *Effect of surfactants*

The effects of surfactants are examined for pinned droplets assuming there is no transport of surfactant to or from the bulk fluids. The key parameters that determine the effect of surfactants are the surface Péclet number $Pe$ (the ratio of convection to diffusion along the interface) and the parameter $\beta$ (a measure of how sensitive the surface tension is to the concentration of surfactant). Strictly speaking, the linear equation of state relating $\beta$ and $\Gamma$ is only valid at low values of $\beta$. However, to obtain a qualitative understanding of the effects of surfactants on the dynamic behaviour and stability of the droplets, a wide range of $\beta$ is examined. Note the capillary number $Ca$ includes the reduction of surface tension due to the initially uniform distribution of surfactant.

Figure 12 shows the concentration of surfactant along the interface for three values

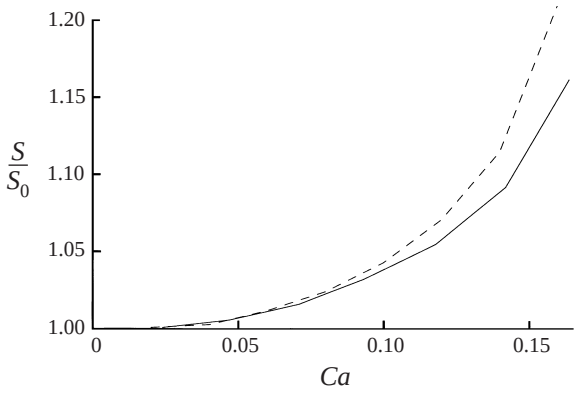


FIGURE 11. Effect of flow regime on droplet deformation versus for droplets of size $A = 0.5,\ \theta = 60^\circ,\ \lambda = 1$. Deformation versus $Ca$ for shear (- - -) and pressure-driven (—) flows.

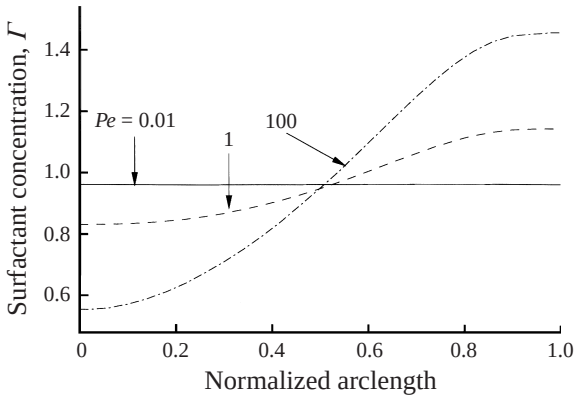


FIGURE 12. Distribution of surfactant along the interface for a droplet in pressure-driven flow with $Ca = 0.1,\ \theta = 60^\circ,\ A = 0.5,\ \lambda = 1,\ \beta = 0.25,\ Pe = 0.01,\ 1,\ 100$.

of $Pe$ for a droplet with $Ca = 0.1$, $A = 0.5$, $\theta = 60$ degrees and $\beta = 0.25$. When $Pe = 0.01$, surface diffusion is the dominant mechanism for surfactant transport on the interface, and therefore the concentration of surfactant remains uniform along the interface. As the interface deforms, the increase in arclength dilutes the surfactant and the concentration is reduced from its initial value of 1.0 to 0.96. For $Pe = 1$, convection and diffusion of surfactant are of comparable importance and convection transports surfactant to the downstream portion of the interface. For $Pe = 100$, convection is the dominant mechanism for surfactant transport, and surfactant is three times more concentrated at the downstream end of the interface relative to the upstream end. Figure 13 illustrates the effect that the surface Péclet number, and hence different distributions of surfactant along the interface, have on the surface velocity. As the surface Péclet number increases, Marangoni stresses generated by the non-uniform distribution of surfactant reduce the surface velocity. This effect was also observed by Borhan & Mao (1992) for the case of freely suspended droplets in a capillary tube.

Figure 14 shows the deformation of the interface as a function of $\beta$ for $Pe = 0.01$, 1 and 100 with $Ca = 0.1$, $\theta = 60^\circ$ and $\lambda = 1$. Increasing $\beta$ for a given value of $Pe$ generally results in a reduction in the deformation of the interface for one of two

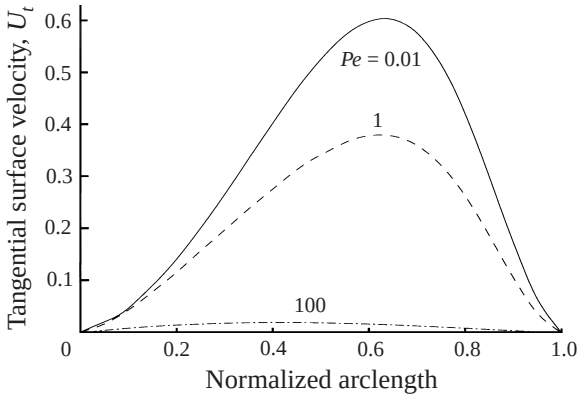


FIGURE 13. Tangential velocity for a droplet in a pressure-driven flow with $Ca = 0.1$, $\theta = 60°$, $A = 0.5$, $\lambda = 1$, $\beta = 0.25$, $Pe = 0.01$, 1, 100.

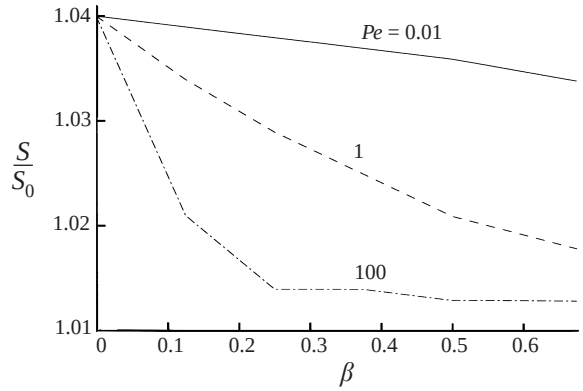


FIGURE 14. Effect of $\beta$ on droplet deformation for $Ca = 0.1$, $\theta = 60$, $A = 0.5$, $\lambda = 1$ and $Pe = 0.01$, 1, 100.

reasons. When $Pe \ll 1$, the surfactant is uniformly distributed along the interface, and there are no Marangoni stresses along it. However, the initial concentration of surfactant $\Gamma = 1$ is diluted due to the increased interfacial area by deformation. The dilution of surfactant on the interface increases the surface tension and hence the surface forces retarding deformation. The effect of dilution becomes more pronounced with increasing $\beta$, and so the deformation decreases. For larger values of $Pe$ and small $\beta$, there is the additional effect that a non-uniform surfactant distribution produces Marangoni stresses along the interface, which reduce deformation. In these cases increasing $\beta$ also increases the magnitude of the Marangoni stresses due to the factor of $1/(1-\beta)$ which appears in equation (2.9). When $\beta$ reaches a sufficiently large value (about 0.25 in figure 14 for $Pe = 100$) the interface becomes immobilized, as shown in figure 13, and the Marangoni stresses reach a plateau. Then the deformation no longer continues as seen in figure 14. Note that the above also explains the increasing critical capillary number with increasing $\beta$ shown in table 1.

Figure 15 illustrates the effect of increasing $Pe$ for two values of $\beta$. The deformation of the droplet is approximately independent of $Pe$ for $Pe < 0.1$ or $Pe > 20$ for both values of $\beta$, where either diffusive transport, in the former case, or convective transport, in the latter case, dominates. As mentioned earlier the decreasing deformation with

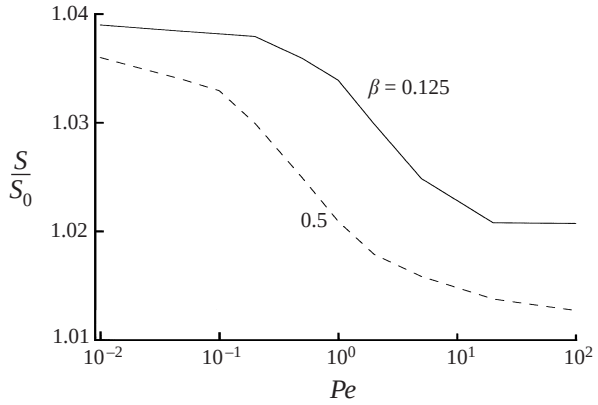


FIGURE 15. Effect of surface Péclet number on droplet deformation. $Ca = 0.1$, $\theta = 60°$, $A = 0.5$, $\lambda = 1$ and $\beta = 0.125$, $\beta = 0.5$.

increasing $Pe$ is due to the increasing Marangoni stresses. However, the critical capillary number is relatively insensitive to $Pe$ as shown in table 1.

In summary, for surfactants to produce a significant difference in the deformation of the interface, the surface tension must be moderately sensitive to the presence of surfactant, i.e. $\beta \geqslant 0.25$, or surface-convection must be dominant, i.e. $Pe \gg 1$.

## 4. Moving contact lines

The no-slip boundary condition at the contact lines is now relaxed to allow the droplet to slip along the wall. The effects of slip on the steady shape and stability of droplets in pressure-driven flow are compared to the results for pinned droplets. Results are presented for surfactant-free droplets for several values of $Ca$, $A$ and $\lambda$. The dynamic behaviour of the droplets is shown in a frame of reference moving with the upstream contact line.

Currently, there is no well established relationship between the contact angle and the velocity of the contact line. Rather than introduce an additional phenomenological relationship, it is assumed here that the contact angle is independent of the speed of the contact line and is therefore equal to its static value. Previously it has been assumed that the contact line does not begin to move until reaching a critical contact angle which is different for the advancing and receding contact lines. If the upstream and downstream contact angles are the same then the droplets necessarily must slip for any ambient flow (Dussan V. 1987). However, any yield criteria, or lack thereof, probably depend on the nature of the solid and liquids composing the system. Unpublished experiments of immiscible droplet displacement in pressure-driven flow that we have done indicate that the droplet slips for all capillary numbers, so here a yield condition for droplet motion is not included. Although the presence of contact angle hysteresis, or equivalently a finite yield stress, could lead to quite different results, only the limit where there is no contact angle hysteresis is examined. In this case the droplet will always move. This contrasts with the results in the previous section, where the droplet is required to remain pinned to its initial position. The deformation and critical capillary numbers for the results of problems where the effects of contact angle hysteresis are included would be expected lie between these two limits.

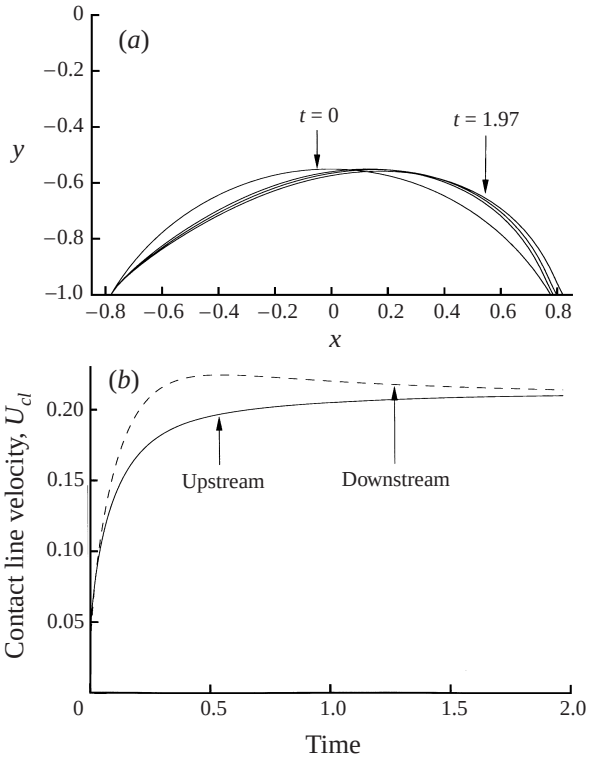


FIGURE 16. Dynamic behaviour for a droplet with moving contact lines at $Ca = 0.1$, $\theta = 60°$, $A = 0.5$, $\lambda = 1$ and $\alpha = 0.2$ (*a*) Evolution of interface at times $t = 0$, 0.30, 0.59 and 1.97. Note the last time corresponds to steady state. (*b*) Evolution of upstream and downstream contact line velocities for sliding droplets. The dynamic behaviour of the droplet is shown in the reference frame moving with the upstream contact line.

For all the simulations presented below, the size of the contact line region $\epsilon = 0.05$ and the slip coefficient $\alpha = 0.2$. The size of the contact line region was chosen to be as small as possible while allowing us to refine the grid and examine the effect of higher order elements. The value of the slip coefficient was chosen so that it corresponded to a Navier-slip coefficient of about $k = 10^{-2}$. Sensitivity studies indicated that decreasing $\alpha$ results in decreased droplet velocities and critical capillary numbers but does not change the qualitative behaviour.

### 4.1. *Dynamic behaviour and effect of contact angle*

Figures 16–18 illustrate the time evolution of sliding droplets with $\lambda = 1$, $A = 0.5$ and $Ca = 0.1$, which is below their critical capillary numbers, along with their corresponding contact-line velocities as a function of time. Initially, the droplets are cylindrical caps which upon application of the pressure-gradient deform and slide along the wall in the flow direction. The relative velocities of the two contact lines and the final translational speed as well as the time required to reach a steady shape all depend on the contact angle.

When $\theta = 60°$ (figure 16*a*, *b*), the contact line velocities diverge soon after the pressure gradient is applied, with the downstream contact line moving more quickly than the upstream contact line and thus increasing the wetted area between the droplet and the wall. The droplet therefore appears to spread along the wall before

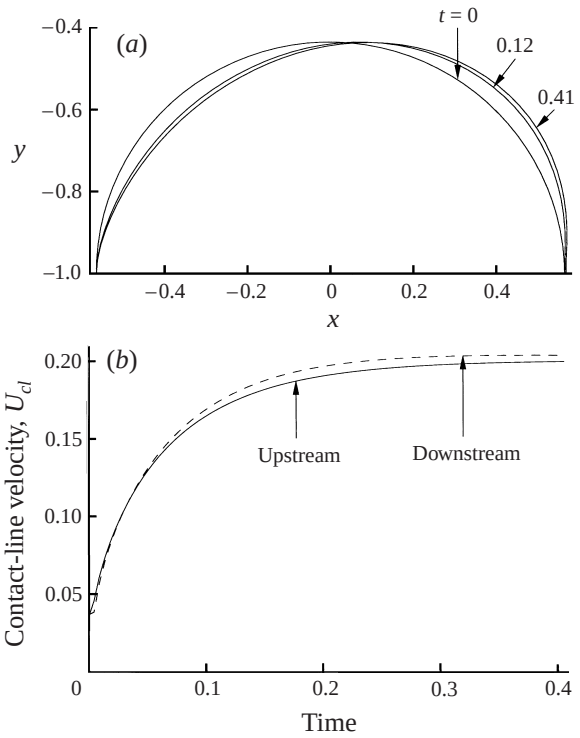


FIGURE 17. As figure 16 but for $\theta = 90°$, and times $t = 0$, 0.12 and 0.41 in ($a$). Note that the last time corresponds to steady state.

reaching a steady shape, when it translates at a constant dimensionless velocity of about 0.21. The dimensional contact-line velocity would be $0.21Eh$, or equivalently, $0.63\,\mathscr{U}h/L$ where $\mathscr{U}$ is the average velocity of the fluid in the channel. The downstream contact-line velocity increases to a maximum value of 0.22 at around $t = 0.5$ and then begins to slow down and reaches its steady value at $t = 1.97$. While the downstream contact line accelerates to a maximum velocity and then begins to slow down, the upstream contact-line velocity monotonically increases with time until it is within 1% of the mean value of the contact-line velocities. Note that reducing the convergence criteria for sliding droplets so that the contact-line velocities are within 0.5% of their mean value does not produce a significant change in the steady shape of the droplet or the contact-line velocities.

When $\theta = 90°$ (figure 17$a, b$) the downstream contact line again moves more rapidly than the upstream contact line and the droplet therefore appears to spread along the wall until a steady shape and translational velocity are reached. In this case the contact line velocities remain fairly close to each other until a steady shape is reached. Consequently, the wetted area does not increase as much as when $\theta = 60°$. The downstream contact-line velocity begins to plateau at around $t = 0.3$, and the upstream contact line reaches its steady value of about 0.19 at $t = 0.41$.

For the case of $\theta = 120°$ (figure 18$a, b$), the downstream contact line moves more slowly than the upstream contact line, and the wetted area between the droplet and wall decreases with time. The downstream contact-line velocity increases rapidly at first and plateaus to a value of about 0.18 near $t = 0.68$. The upstream contact

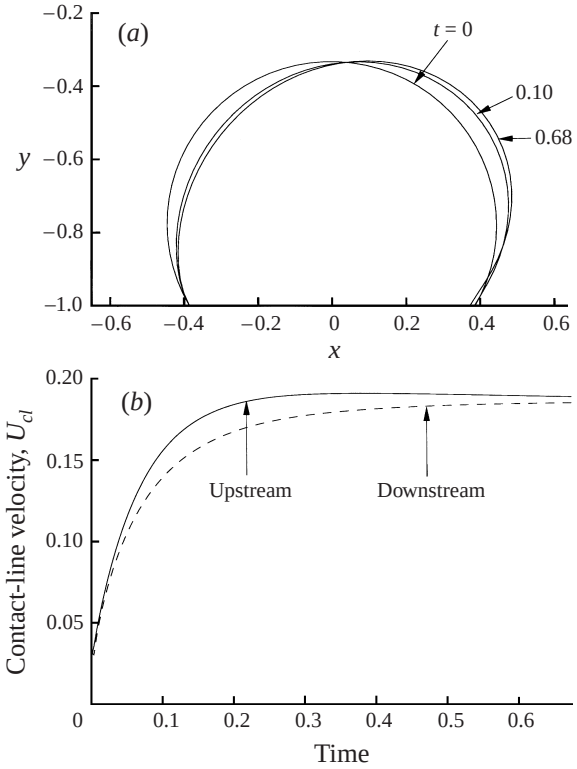


FIGURE 18. As in figure 16 but for $\theta = 120°$, and times $t = 0$, 0.10 and 0.68. Again the last time corresponds to steady state.

line velocity increases more rapidly than the downstream contact line and begins to plateau at around $t = 0.25$.

### 4.2. *Effect of Ca*

Figure 19(*a*) shows the typical deformation of a droplet for several values of *Ca* for $\theta = 60°$. Increasing the capillary number leads to an increase in the wetted area between the droplet and the wall. As the wetted area increases, the height of the droplet decreases to conserve mass. Comparing these steady droplet shapes with those of droplets with pinned contact lines, sliding droplets show only a slight depression in the upstream portion of the interface at the highest value of the capillary number, whereas when the contact lines are pinned the depression is much more pronounced and occurs at a lower capillary number. There are several reasons for these differences. First, the droplet height is decreasing with increasing capillary number, thus the droplet is not influenced as much by the ambient parabolic velocity field. Second, when the contact lines are allowed to slip, the contact angles at the upstream and downstream contact lines are fixed. This does not allow the region of the interface near the contact lines to deform as much as when the contact lines are pinned. Finally, since the droplets are sliding along the solid, the relative velocity between the ambient fluid and the interface is reduced, thus lowering the effective capillary number. As was observed for droplets with pinned contact lines, the lower capillary number simulations do not show as large a depression in the upstream portion of the interface. Figure 19(*b*) illustrates the dependence of the

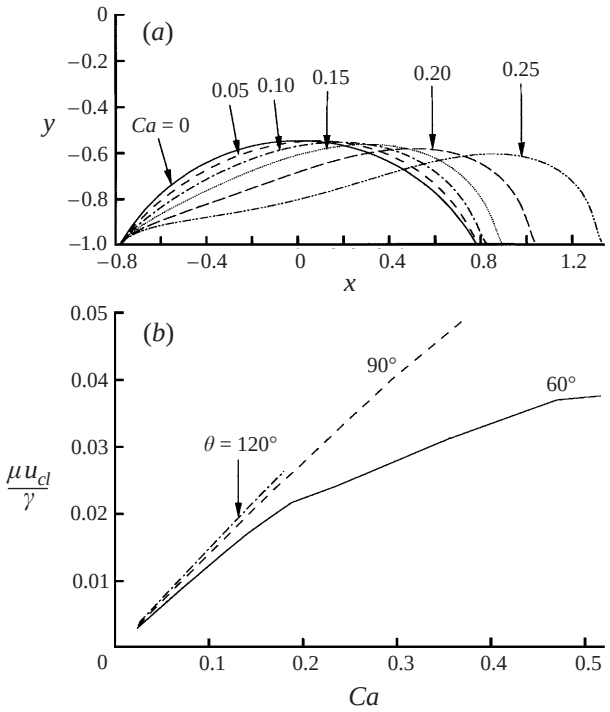


FIGURE 19. (*a*) Steady-state interfaces of droplets with moving contact lines for $\theta = 60°$, $A = 0.5$, $\lambda = 1$, $\alpha = 0.2$ and $Ca = 0$, 0.05, 0.10, 0.15, 0.20, 0.25. (*b*) Dependence of steady-state value of the dimensionless contact line velocity $\mu u_{cl}/\gamma$ on $Ca$ for $\theta = 60°$, 90°, and 120°.

steady-state value of the dimensionless contact-line velocity $\mu u_{cl}/\gamma$ on $Ca$. Generally, as $Ca$ increases the droplet translates more rapidly. For $\theta = 90°$ or 120° the contact-line velocity is linear in $Ca$. However, for $\theta = 60°$, there are two regions where the contact-line velocity varies linearly. The transitions between these regions correspond to significant changes in the height of the droplet as seen in figure 19(*a*). Note that the end of each curve corresponds to the critical capillary number.

Figure 20 illustrates the time evolution of the interfaces of droplets above their critical capillary numbers. The dynamic behaviour of the droplet is shown in the reference frame moving with the upstream contact line. When $\theta = 60°$ and $Ca = 0.5$ (figure 20*a*) the downstream contact line moves faster than the upstream contact line and the droplet appears to spread along the wall. The upper portion of the droplet deforms and translates more rapidly than the lower portion and eventually pinches off. When $\theta = 90°$ and $Ca = 0.6$ (figure 20*b*), the downstream contact line moves more slowly than the upstream contact line, the opposite of what happens below the critical capillary number, and the interface continues to deform, eventually pinching off a larger droplet which is entrained into the bulk flow and leaving a smaller droplet attached to the wall. When $\theta = 120°$ and $Ca = 0.5$ (figure 20*c*), the downstream contact line again moves more slowly than the upstream contact line and it appears that the contact lines may eventually come together and thus the entire droplet would detach from the wall. Unfortunately, the numerical method does not include the coalescence of the contact lines. This illustrates the general trend that above the critical capillary number increasing the contact angle results in a larger fraction of droplet being entrained in the bulk. Including the effects of contact angle hysteresis

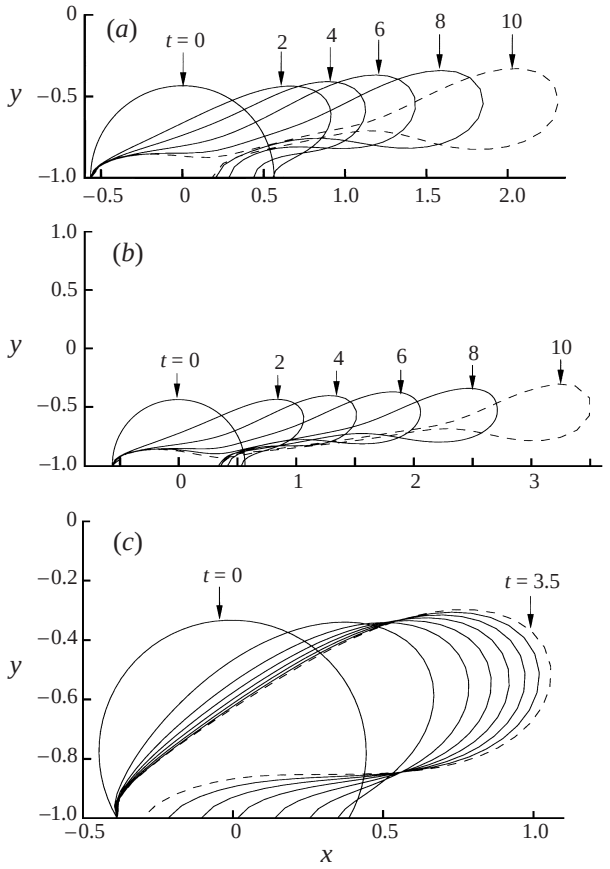


FIGURE 20. Dynamic behaviour of droplets with moving contact lines above the critical capillary number for $A = 0.5$, $\lambda = 1$ and $\alpha = 0.2$ at evenly spaced time intervals from (*a*) $t = 0$ to $t = 10$ for $Ca = 0.5$, $\theta = 60°$, (*b*) from $t = 0$ to 10 for $Ca = 0.6$, $\theta = 90°$ and (*c*) from $t = 0$ to 3 and $t = 3.5$ for $Ca = 0.5$, $\theta = 120°$. The dynamic behaviour of the droplet is shown in the reference frame moving with the upstream contact line.

may significantly change the results. For example, if the upstream and downstream contact angles were distributed asymmetrically about the static contact angle, then the contact line which yields first will have a more pronounced effect on the dynamics and stability of the droplet.

Figure 21 shows the deformation of the droplet over a range of $Ca$ for contact angles of $\theta = 60°$, $90°$ and $120°$. The end of each curve corresponds to the critical capillary number beyond which no steady state exists and the droplet continues to deform until the droplet pinches off. These numbers are listed in table 2. Comparing figure 21 with figure 4, note that the critical capillary number and the magnitude of the deformation is different for sliding and pinned droplets. Sliding droplets deform less than pinned droplets at the same capillary number because, as noted above, the relative velocity of the fluid along the interface is somewhat lower when the droplet is sliding which lowers the effective capillary number. The critical capillary number for a sliding droplet is higher than for a pinned droplet when $\theta = 60°$ ($Ca_{crit} = 0.52$ versus 0.16) or $\theta = 90°$, ($Ca_{crit} = 0.37$ versus 0.22). However, for $\theta = 120°$ the critical capillary for a sliding drop is 0.18 versus a value of 0.26 for a pinned droplet.

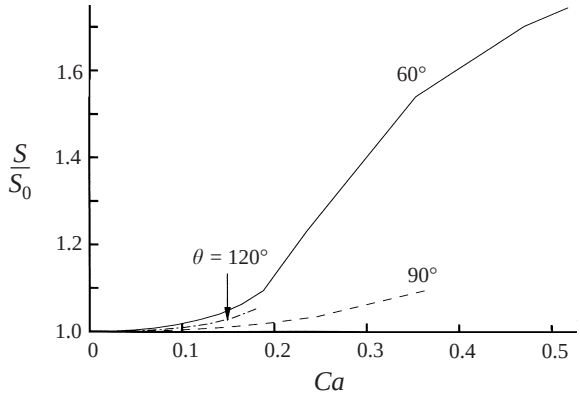


FIGURE 21. Effect of $Ca$ on deformation of droplets with moving contact lines. Deformation versus $Ca$ for $\theta = 60^\circ$, $\theta = 90^\circ$ and $\theta = 120^\circ$.

If the change in the relative fluid velocity over the droplet were the only reason for the change in the critical capillary number, then a greater critical capillary number for all sliding droplets compared to pinned droplets would be expected. Indeed, if the capillary number is corrected for the fact that the droplet is sliding, i.e. $Ca^* = \mu(U - u_{cl})/\gamma$ where $u_{cl}$ is the mean contact-line velocity, then the critical capillary numbers for sliding droplets are closer to those for pinned droplets when $\theta = 60^\circ$ or $\theta = 90^\circ$. However, this correction makes the discrepancy between the capillary numbers worse for droplets with $\theta = 120^\circ$.

Therefore, another effect must be at work here. Other things being equal, droplets with larger contact angles penetrate more deeply into the flow as they slide and deform and experience greater hydrodynamic forces that increase deformation and tend to destabilize the interface. As seen in figures 16($a$) and 17($a$), the wetted area increases and the height decreases to conserve mass for $\theta = 60^\circ$ and $90^\circ$, which stabilizes the interfaces. However, as figure 18($a$) illustrates, when $\theta = 120^\circ$, the wetted area between the droplet and the wall decreases and hence the height of the droplet increases, which destabilizes its interface and dominates the stabilizing effect of the reduction in the relative velocity between the droplet and the bulk flow.

### 4.3. *Effect of viscosity ratio and droplet size*

Table 2 summarizes the effects of viscosity ratio and droplet size on the stability of sliding droplets. Similar to pinned droplets, increasing the area of a droplet decreases its critical capillary number due to an increase in the viscous forces. The effect of the viscosity ratio on the critical capillary number for sliding droplets, however, is more complex than for pinned droplets. For $\theta = 60^\circ$ the critical capillary numbers are 0.59, 0.52 and 0.75 for $\lambda = 0.125$, 1 and 8. For $\lambda < 1$, the critical capillary number is larger because the viscous stresses along the surface of the droplet are smaller. For $\lambda > 1$, the viscous stresses acting on the droplet are larger, but this increases the droplet velocity and its stability by reducing its relative velocity. This is unlike pinned droplets where an increase in the viscosity ratio reduces the stability of the droplet. For $\theta = 120^\circ$, a similar trend is observed, though the critical capillary number is not very sensitive to the viscosity ratio.

| $Ca_{crit}$ | $\theta$ (deg.) | $\lambda$ | $A$ |
|---|---|---|---|
| 0.52 | 60 | 1.0 | 0.5 |
| 0.37 | 90 | 1.0 | 0.5 |
| 0.18 | 120 | 1.0 | 0.5 |
| 0.58 | 60 | 1.0 | 0.25 |
| 0.51 | 60 | 1.0 | 1.0 |
| 0.21 | 120 | 1.0 | 0.25 |
| 0.18 | 120 | 1.0 | 1.0 |
| 0.59 | 60 | 0.125 | 0.5 |
| 0.75 | 60 | 8.0 | 0.5 |
| 0.23 | 120 | 0.125 | 0.5 |
| 0.23 | 120 | 8.0 | 0.5 |

TABLE 2. Effect of contact angle $\theta$, viscosity ratio $\lambda$ and droplet area $A$ on the critical capillary number $Ca_{crit}$ for sliding droplets in pressure-driven flow.

## 5. Conclusions

In this paper the boundary-integral method was used to numerically study the displacement of a two-dimensional droplet attached to a solid surface when inertial and gravitational forces are negligible. It was shown that as the capillary number was increased, the deformation of the droplet increased until a critical value was reached after which no steady droplet shapes were observed. Increasing the droplet size resulted in an increase in the deformation of the interface at a given capillary number since more fluid must flow through an increasingly smaller gap between the droplet and the upper plate. Also, the deformation of the droplet increased as the viscosity ratio was increased up to a point beyond which the viscosity ratio can be considered to be infinite. Shear and pressure-driven flow regimes were examined and shown to have similar values of the critical capillary number.

Surfactants were shown to reduce deformation for pinned droplets as the surface Péclet number was increased for a given value of $\beta$. Marangoni stresses generated by a non-uniform distribution of surfactant act to reduce the surface velocity and lead to a stiffening of the interface. Increasing $\beta$ was shown to reduce the droplet deformation as a result of the increase in the Marangoni stresses and a dilution of the surfactant along the interface.

Relaxing the no-slip boundary condition and allowing the droplet to slip was shown to produce lower values for the deformation of the interface. When $\theta = 60^\circ$ or $90^\circ$ the critical capillary numbers were greater than for pinned droplets due to the lower relative velocity between the bulk flow and the droplet. When $\theta = 120^\circ$ the critical capillary number was less than for pinned droplets because the mode of instability is the coalescence of the contact lines as opposed to large deformations of the droplet.

The boundary-integral method presented here is not limited to studying problems with flat solid boundaries. It is possible to study the effects that wavy walls have on the stability of attached droplets; one particularly interesting question would be whether a sliding droplet could escape a deep groove in the wall.

We would like to thank the reviewers for their helpful and insightful comments. This work was partially supported by NSF Grant CTS 9358409 and a fellowship for R. T. B. from the Packard Foundation.

## REFERENCES


Borhan, A. & Mao, C.-F. 1992 Effect of surfactants on the motion of drops through circular tubes. *Phys. Fluids* A **4**, 2628–2640.

Cox, R. G. 1986 The dynamics of the spreading of liquids on a solid surface. Part 1. Viscous Flow. *J. Fluid Mech.* **168**, 169–194.

Dimitrakopoulos, P. & Higdon, J. J. L. 1997 Displacement of fluid droplets from solid surfaces in low-Reynolds-number shear flows. *J. Fluid Mech.* **336**, 351–378.

Dussan V., E. B. 1979 On the spreading of liquids on solid surfaces: static and dynamic contact angles. *Ann. Rev. Fluid Mech.* **11**, 205–222.

Dussan V., E. B. 1985 On the ability of drops or bubbles to stick to non-horizontal surfaces of solids. Part 2. Small drops or bubbles having contact angles of arbitrary size. *J. Fluid Mech.* **151**, 1–20.

Dussan V., E. B. 1987 On the ability of drops to stick to surfaces of solids. Part 3. The influences of the motion of the surrounding fluid on dislodging drops. *J. Fluid Mech.* **174**, 381–387.

Dussan V., E. B. & Chow, R. T.-P. 1983 On the ability of drops or bubbles to stick to non-horizontal surfaces of solids. *J. Fluid Mech.* **137**, 1–29.

Feng, J. Q. & Basaran, O. A. 1994 Shear flow over a translationally cylindrical bubble pinned on a slot in a plane wall. *J. Fluid Mech.* **275**, 351–378.

Furmidge, C. G. L. 1962 Studies at phase interfaces. I. The sliding of liquid drops on solid surfaces and a theory for spray retention. *J. Colloid Interface Sci.* **17**, 309–324.

Haley, P. J. & Miksis, M. J. 1991 The effect of the contact line on droplet spreading. *J. Fluid Mech.* **223**, 57–81.

Hocking, L. M. & Rivers, A. D. 1982 The spreading of a drop by capillary action. *J. Fluid Mech.* **121**, 425–442.

Li, X. & Pozrikidis, C. 1996 Shear flow over a liquid drop adhering to a solid surface. *J. Fluid Mech.* **307**, 167–190.

Lowndes, J. 1980 The numerical simulation of the steady movement of a fluid meniscus in a capillary tube. *J. Fluid Mech.* **101**, 631–646.

Manga, M. 1996 Dynamics of drops in branched tubes. *J. Fluid Mech.* **315**, 105–117.

Milinazzo, F. & Shinbrot, M. 1988 A numerical study of a drop on a vertical wall. *J. Colloid Interface Sci.* **121**, 254–264.

Muldowney, G. P. 1989 Simulation of time-dependent free-surface Navier–Stokes flows. PhD thesis, University of Illinois at Urbana-Champaign.

Occhialini, J. M., Muldowney, G. P. & Higdon, J. J. L. 1992 Boundary integral/spectral element approaches to the Navier–Stokes equations. *Intl J. Numer. Meth. Fluids* **15**, 1361–1381.

Pozrikidis, C. 1992 *Boundary Integral and Singularity Methods for Linearized Viscous Flow*. Cambridge University Press.

Stone, H. A. 1990 A simple derivation of the time-dependent convective-diffusion equation for surfactant transport along a deforming interface. *Phys. Fluids* A **2**, 111–112.

Tanzosh, J., Manga, M. & Stone, H. A. 1992 In *Proc. Boundary Element Technologies VII* (ed. C. A. Brebbia & M. S. Ingber), pp. 19–39. Computational Mechanics Publications.

Tilton, J. N. 1988 The steady motion of an interface between two viscous liquids in a capillary tube. *Chem. Engng Sci.* **43**, 1371–1384

Tsai, T. M. & Miksis, M. J. 1994 Dynamics of a drop in a constricted capillary tube. *J. Fluid Mech.* **274**, 197–221.

Tuck, E. O. & Schwartz, L. W. 1991 Thin static drops with a free attachment boundary. *J. Fluid Mech.* **223**, 313–324.

Zhou, H. & Pozrikidis, C. 1991 Pressure-driven flow of suspensions of liquid drops. *Phys. Fluids* **6**, 80–93.

Zhou, M.-Y. & Sheng, P. 1990 Dynamics of immiscible-fluid displacement in a capillary tube. *Phys. Rev. Lett.* **64**, 882–885.